ISSN 0022-4766, Journal of Structural Chemistry, 2020, Vol. 61, No. 2, pp. 207-224. © Pleiades Publishing, Ltd., 2020.
Text © The Author(s), 2020, published in Zhurnal Strukturnoi Khimii, 2020, Vol. 61, No. 2, pp. 221-238.

MOLECULAR STRUCTURAL PROPERTIES OF [*n*]-ANNULENE (*n* = 8, 10, 12, 14) AND ITS BORON NITRIDE DERIVATIVES: ANALYSIS OF NMR, NBO, ELF AND PDI*

M. Monajjemi[1] and F. Mollaamin[1]**

Due to the importance of structural properties of annulene in physical and inorganic chemistry, the trajectory of the NBO to MO evolution can be written as natural atomic orbitals (NAO) → natural hybrid orbital (NHO) → natural bond orbital (NBO) → natural semi-localized MO (NLMO) → MO. The electron density distribution in this [*n*]-annulene series (both ions and molecules) (*n* = 8, 10, 12, 14) is investigated by NMR, NBO, ELF, FLU, and PDI analyses. The (4*n*+2)π and also 4*n*π systems (Hückel′s rule) on variants of those compounds via the localized orbital localization (LOL) and electron localized function (ELF) are discussed, and a diatropic ring current (aromatic) is also distinguished for some other paratropic currents (anti-aromatic). The NHO direction and bond bending deviations from the line of nuclear centers are exhibited for understanding the situation of π and σ orbitals. In this work, for each NAO function, core, valence, or Rydberg, the orbital occupancy and the orbital energies are discussed. In addition, nucleus independent chemical shifts (NICSs) and statistical nucleus chemical shifts (S-NICSs) confirm the aromaticity and anti-aromaticity amounts in those rings.

DOI: 10.1134/S0022476620020055

Keywords: aromaticity, LOL, ELF, annulene structures, current density induced, paratropic, diatropic.

INTRODUCTION

Annulene belongs to a series of conjugated monocyclic hydrocarbons with the common formula C_nH_n (*n* = even) or C_nH_{n+1} (*n* = odd), such as benzene ([6]-annulene), cyclobutadiene ([4]-annulene), cyclooctatetraene ([8]-annulene), and cyclotetradecaheptaene ([14]-annulene). Annulenes may be non-aromatic ([10]), anti-aromatic ([12]), or aromatic ([6]-annulene). Cyclooctatetraene (COT) or [8]-annulene, which is a poster child for non-aromatic molecules, was first synthesized by Richard Willstatter [1]. The coupling between COT^{2-} charge states and their mechanical conformations constructs a new position for COT^{2-} as an aromatic molecule, including the electromechanical converter treatment. Planar conjugated COT^{2-} exhibits a powerful link between π-electrons in its molecular structure. Huckel′s "4*n*+2" rule indicates a monoaromatic ring from anti-aromatics with their magnetic properties.

[1]Department of Chemical Engineering, Central Tehran Branch, Islamic Azad University, Tehran, Iran; **m_monajjemi@yahoo.com. Original article submitted July 22, 2019; revised September 5, 2019; accepted September 6, 2019.

*Supplementary materials are available for this article at doi 10.1134/S0022476620020055 and are accessible for authorized users.

Although COT that follows a non-planar conformation with alternating double and single bonds via the D_{2d} symmetry is not an aromatic molecule, the $C_8H_8^{2-}$ dianion (cyclooctatetraenide) is an aromatic ion with a suitable resonance energy. This dianion is planar, octagonal in its structure, and aromatic with the Huckel electron count of 10. Through the interaction between the alternating bonds, it has been confirmed that the COT structures undergo a thermal shift bonding and ring inversion operations, including a D_{4h} planar transition state [2-7]. In addition, the NMR data [2] indicate that the COT dianion (COT^{2-}) adopts a D_{8h} symmetry structure. Although the planar D_{4h} structure for the ring inversion of COT has a transition state (TS) with a barrier energy around 12 kcal/mol [8-10], the D_{8h} bond switching TS lays higher by a few kcal/mol. Actually, COT has three fundamental structural changes, including 1-ring inversions, 2-bond shifts, and 3-valences isomerization (Scheme 1) [11-13].

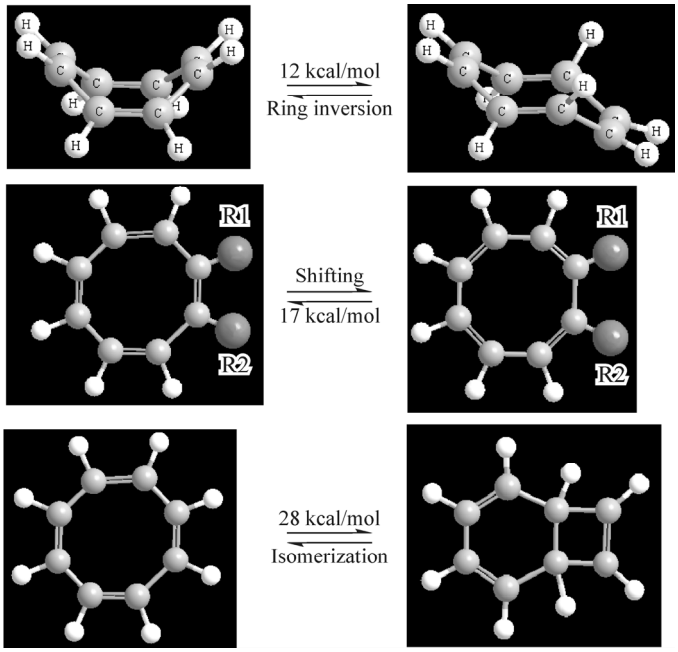

Scheme 1. Structural changes in cyclooctatetraene, including ring inversion, shifting, and valence bond isomerization.

Studies of several annulene molecules such as C_8H_8, $C_{10}H_{10}$, $C_{12}H_{12}$, $B_7N_7H_{14}$, and $C_{16}H_{16}$ help to explain the details of the mentioned magnetic mechanism concerning the ring induced currents related to the aromaticity behavior (Scheme 2).

Steiner and Fowler investigated a model via frontier orbital contributions, which yields an accurate result of π ring currents in benzene, COT^{2-}, $B_4N_4H_8^{2-}$, and such other planar rings [14, 15]. London [16], Pauling [17], and Pople [18] investigated the concept of aromaticity and anti-aromaticity in the viewpoint of the magnetic criterion, diatropic (planar of $4n$+2 systems) and paratropic currents (planar of $4n$ systems). Schleyer and coworkers in 1996 showed that the ring current was an outcome of the HOMO–LUMO transition depending on symmetry properties and localized current-density circulations around the electronegative nucleus [19]. For the $C_8H_8^{n+2}$ ($n = -4, -2$) and $B_nN_nC_{8-2n}H_8$ ($n = 1, 2, 4$) systems, density maps exhibit the π electrons with the localized circulations around the electronegative nucleus. It has been illustrated that the spread of virtual orbitals can help compute currents in carbocyclic aromatic rings.

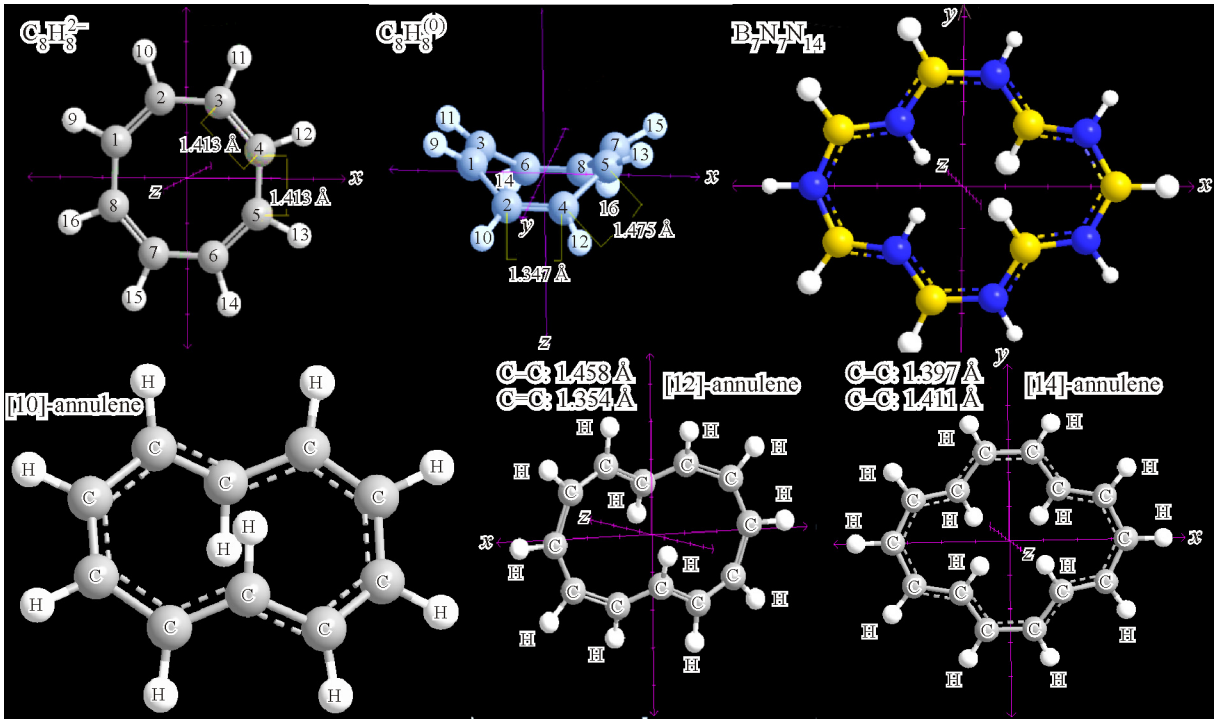

Scheme 2. Optimized geometries of variants of [*n*]-annulene (*n* = 8, 10, 12, and 14) and its aza-boron derivatives such $B_7N_7H_{14}$.

THEORETICAL

Induced current densities. The theory of induced current densities has been investigated by Steiner via discussions of the "ipsocentric" approach [14, 15] which leads to a normal description of molecular orbital contributions. With supposing a closed shell of *N*-electron systems with pair-occupied orbitals ψ_n (which are Hartree–Fock orbitals) and ψ_p as unoccupied orbitals, in a constant magnetic field **B**, the Hamiltonian is defined as

$$\hat{H} = \hat{H}_0 + \frac{e^2}{2m_e}\hat{I}(d)\cdot\mathbf{B}, \tag{1}$$

where $\hat{I}(d)$ is the angular momentum related to the momentum operator of

$$(\hat{p}): \hat{I}(d) = (r-d)\cdot\hat{P}. \tag{2}$$

Consequently, the induced current density "$J^{(1)}(r)$" is a summation of two terms which can be written for the full occupied orbital $\{\psi_n\}$ as follows [14, 15]:

$$j_n(r) = \frac{-e^2}{m_e}\mathbf{B}\cdot(r-d)\psi_n^2(r) + \frac{2ie\hbar}{m_e}[\psi_n(r)\nabla\psi_n^{(1)}(r) - \psi_n^{(1)}(r)\nabla\psi_n(r)]. \tag{3}$$

The first term indicates diamagnetic current densities ($\{j_n^{dia}(r)\}$), which is related to the density of unperturbed orbitals, and the secondary term indicates paramagnetic current densities $\{j_n^{pra}(r)\}$. Although there is no physical interpretation for this segregation of diamagnetic and paramagnetic parts, usually systems break down in two diamagnetic-paramagnetic parts, of course, in complete basis sets. As described in [15], the correction to each occupied orbital is a sum over the occupied orbitals to unoccupied orbitals $\{\psi_p(r)\ (P > (N/2))\}$. Therefore, $\psi_n(r)$ for one electron can be written as follows:

$$\psi_n(r) = \frac{-e^2}{2m_e}\left[\sum_{p>(N/2)}\psi_n(r)\frac{\langle\psi_p \mid \hat{I}(0) \mid \psi_n\rangle}{\varepsilon_p - \varepsilon_n}\right]\cdot\mathbf{B} + \frac{e^2}{2m_e}\left[d\cdot\sum_{p>(N/2)}\psi_p(r)\frac{\langle\psi_p \mid \hat{P} \mid \psi_n\rangle}{\varepsilon_p - \varepsilon_n}\cdot\mathbf{B}\right]. \quad (4)$$

The first term is $\{\psi_n^{pra}(r)\}$ and $\psi_p \mid \hat{I}(0) \mid \psi_n$ is the rotational transition angular momentum between energy differences $\varepsilon_p - \varepsilon_n$ from unoccupied orbitals towards occupied orbitals. The second summation $\{\psi_n^{dia}(r)\}$ and $\psi_p \mid \hat{P} \mid \psi_n$ is a linear momentum of those transition energies.

Ring current towards aromaticity. Aromaticity can be defined through magnetic criteria and is a trustworthy account of induced currents through external magnetic capabilities. In addition, chemical shift, isotropy, anisotropy, span, asymmetry, and other properties are all integrals of these current densities. Moreover, the current density map can be estimated by theoretical methods without any gauge-dependence problem. Meanwhile, from occupied to unoccupied orbitals, the total current densities which are modulated and governed by energy divisors and symmetry rules, respectively, are evaluated. Symmetry including T_x and T_y transitions for both occupied and unoccupied orbitals (without R_z) is related to the diatropic concept while this contribution to the R_z symmetry (without T_x and T_y) has paratropic behavior [20]. For the magnetic pattern, the outcome of all such components explains the aromaticity or anti-aromaticity, which is related to the net diatropicity and paratropicity of the ring currents, respectively.

Isotropic and anisotropic parameters. Total chemical shift tensors σ are non-symmetrical tensors which can be separated through three independent parameters which are known as isotropic, traceless symmetric, and traceless anti-symmetric [21]. In addition, a spherical tensor has been described by Haeberlen [22], Mehring [23], and Diehl [24]. They have investigated fundamental tensors as

$$\sigma = \sigma^{\mathrm{iso}(0)} + \sigma^{\mathrm{anti}(1)} + \sigma^{\mathrm{sym}(2)}. \quad (5)$$

Spherical tensors can also be written as

$$\sigma_0^{\mathrm{iso}(2)} = \sqrt[2]{\frac{3}{2}}\delta_{(zz)} \quad \text{and} \quad \sigma_{\pm 2}^{\mathrm{sym}(2)} = \frac{1}{2}\delta_{(zz)}, \quad (6)$$

where δ_{zz} is the reduced anisotropy and can be calculated through

$$[\delta_{zz} = (\sigma_{zz} - \sigma_{\mathrm{iso}}) = (\sigma_{33} - \sigma_{\mathrm{iso}})]. \quad (7)$$

This parameter is related to the anisotropy ($\Delta\sigma$) with

$$\Delta\sigma = \frac{3}{2}\delta_{(zz)}. \quad (8)$$

From equations (7) and (8), the asymmetry (η) shielding can be estimated as

$$\Delta\sigma = \delta_{zz} - \frac{1}{2}(\delta_{xx} + \delta_{yy}). \quad (9)$$

and [25]

$$\eta = \left(\frac{\delta_{yy} - \delta_{xx}}{\delta_{(zz)}}\right) = \frac{3(\delta_{yy} - \delta_{xx})}{2\Delta\sigma}. \quad (10)$$

The magnetic resonance of the spins are seldom isotropic, therefore, they represent new tensors (Herzfeld–Berger notation) [26]. These tensors are known as Span (Ω) $\Omega \geq 0$, which illustrates the maximum width of the model and the skew (κ) of the tensors that are

$$(\Omega) = \sigma_{33} - \sigma_{11} \quad \text{and} \quad \kappa = \frac{3(\delta_{\mathrm{iso}} - \delta_{22})}{\Omega}. \quad (11)$$

Moreover, the skew orientation (κ) is given by

$$\kappa = \frac{3(\delta_{1so} - \delta_{22})}{\Omega}, \quad (-1 \le \kappa \le +1). \tag{12}$$

In some items, an axially symmetric tensor ($\sigma_{yy} - \sigma_{xx}$) might be zero and therefore $\eta = 0$. In addition, the asymmetry (η) indicates how great deviation can appear from the axially symmetrical tensors, so the region of "η" is between zero and one ($0 \le \eta \le +1$).

Current electron density, ELF and LOL functions. The current densities can be rearranged as

$$\rho(r) = \eta_i \mid \varphi_i(r) \mid^2 = \sum_i \eta_i \mid \sum_i C_{l,i}\chi_i(r) \mid^2 . \tag{13}$$

Here χ is the basis function of orbitals and η_i is the occupation number. C is also a coefficient matrix. Bader [27] revealed that large electron localization regions have a wide Fermi hole. Becke and coworkers [28] illustrated that a spherically average like-spin pair has a suitable correlation with the Fermi hole. Consequently, they introduced a new function as ELF.

$$\mathrm{ELF}(r) = \frac{1}{1 + [D(r)/D_0(r)]^2}, \tag{14}$$

where

$$D(r) = \frac{1}{2}\sum_i \eta_i \mid \nabla\varphi_i \mid^2 - \frac{1}{8}\left[\frac{\mid \nabla\rho_\alpha \mid^2}{\rho_\alpha(r)} + \frac{\mid \nabla\rho_\beta \mid^2}{\beta(r)}\right] \tag{15}$$

and

$$D_0(r) = \frac{3}{10}(6\pi^2)^{2/3}[\rho_\alpha(r)^{5/3} + \rho_\beta(r)^{5/3}] \tag{16}$$

for closed-shell systems, since $\rho_\alpha(r) = \rho_\beta(r) = 1/2\rho$. D and D_0 terms can be simplified as

$$D(r) = \frac{1}{2}\sum_i \eta_i \mid \nabla\varphi_i \mid^2 - \frac{1}{8}\left[\frac{\mid \nabla\rho \mid^2}{\rho(r)}\right] \tag{17}$$

and

$$D_0(r) = \frac{3}{10}(3\pi^2)^{2/3}\rho(r)^{5/3}. \tag{18}$$

Savin et al. [29] indicated which $D(r)$ determined the excess kinetic energies due to the Pauli repulsion, while $D_0(r)$ has been known as the Thomas–Fermi kinetic energy term. In other words, they reconsidered ELF in the viewpoint of kinetic energy through the Kohn–Sham DFT wave function. Therefore, ELF would be in the range [0, 1] and a large ELF value indicates that electrons are strongly localized. ELF is used for wide varieties of molecules such as organic, inorganic, atomic crystals, coordination compounds, clusters, and also aromatic rings. The LOL is another function similar to ELF investigated by Becke and coworkers [30].

$$\mathrm{LOL}(r) = \frac{\tau(r)}{1 + \tau(r)},$$

where

$$(r) = \frac{D_0(r)}{\frac{1}{2}\sum_i \eta_i \mid \nabla\varphi_i \mid}, \tag{19}$$

$D_0(r)$ for both spin-polarized and closed shell systems are explained with the same meaning as in ELF. Jacobsen [31] showed that LOL supplied a more definite and obvious image than ELF. Therefore, LOL can be better interpreted in kinetic energies than ELF. As for LOL, it can also be interpreted in the viewpoint of localized orbitals. The LOL values are similar to those of ELF: between zero and one [0, 1].

NBO analysis. Electron delocalization can be defined based on the Lewis amount. It can be considered that the maximum electronic charges on the Lewis orbitals has a low electronic charge, corresponding to strong electron delocalization effects. In the resonance phenomenon, major and minor percentage combinations may appear in several calculations. Based on perturbation theories of the Fock matrix, it is possible to estimate the donor-acceptor (bonding with anti-bonding) interactions in the NBO analysis. These analyses are carried out through examining all possible interactions among donor Lewis-types (filled) with acceptor (empty) non-Lewis NBOs. The estimation of their energies is calculated based on second order perturbation theory. Since these interactions are related to the donation of occupancies from the localized to the idealized Lewis structure into the empty non-Lewis orbitals, they are introduced as delocalization corrections to the zero-order natural Lewis structures. For any donor (i) and acceptor (j), the stabilization energies E^2 are associated with delocalization. The equation exhibits the relation of the F matrix as follows:

$$E^2 = \Delta E_{ij} = q_i \frac{F_{i,j}^2}{\varepsilon_j - \varepsilon_i},$$

where q_i are the donor occupancies and $\varepsilon_j - \varepsilon_I$ are diagonal orbital energies. In addition, $F_{i,j}^2$ is known as the Fock matrix function.

Computational details

The geometry and electronic structures have been obtained by advanced DFT methods using M06-2X and CAM-B3LYP series of functionals. These methods are based on the solution of Kohn–Sham orbitals [32] and the Perdew exchange-correlation functional [33]. The geometry of each part of ions was optimized by various methods, including cc-pVDZ and cc-pVTZ with CAM-B3LYP DFT. DFT calculations were accomplished to obtain the current ring data for $4n$ and $4n$+2 molecules of [n]-annulene (n = 8, 10, 12, and 14) and its aza-boron derivatives. Induced currents were calculated using the LEF and LOL approaches, which indicate planar structures with the D_{4h} symmetry for some variants of $C_8H_8^{n+2}$ (n = –4, –2, 0) and $B_7N_7H_{14}$-annulene at these levels of theory. For drawing the contour line maps of current densities, the Multiwfn software has been used [34, 35] for the planar and fully optimized structures. The contour lines of electron densities have been plotted based on Bader′s theory [27]. These plots are needed for analyzing the electrostatic potential surface distribution for each of the ions. These contour lines have been plotted in gradient line maps through the same items. The relief maps were applied for presenting the height data at each center. Shaded surface maps with and without projections are applied to represent the height values at each position. To confirm the data, several extra calculations, including MP_4 (SDQ)/6-31+G(d'), QCISD(T)/6-31+G(d'), and CAM-B3LYP/6-311G, have also been made. Charge transfers were also evaluated using Merz [36], chelp or chelpG [37, 38]. Those methods are based on the charge fitting of electrostatic potential approaches (MESP) suitable for small molecules [39-46]. Electron densities, values of orbitals, LUMO and HOMO orbitals, electrons spin densities, electrostatic charges, ELF, LOL, and total electrostatic potential (ESP) have also been calculated in this work using the Multifunctional Wave-function analyzer [34, 35].

Among the several methods and basis sets applied in this work, cc-pVDZ and cc-pVTZ yield the most desirable results for the ESP fitting. All ab initio calculations were performed using GAMESS-US and the optimization was made along with the frequency calculations to confirm that the geometries were indeed optimal with no imaginary frequencies.

RESULTS AND DISCUSSION

Geometry properties and optimized energies of [n]-annulene (n = 8, 10, 12, and 14) and its aza-boron derivatives obtained by various methods are listed in Table 1. It has been shown that the advanced DFT method, including CAM-B3LYP/cc-pVDZ and M06-2X/cc-pVTZ, give accurate results of negative energies, relative stabilities, C–C and C–H bond lengths, and gap energies as compared to other methods, therefore, these two methods have been selected for the investigation and calculation of the other variants of those molecules (Table 1). It is now generally agreed that homologues

TABLE 1. Geometry and Energy of [n]-Annulene (n = 8, 10, 12, and 14) and its Aza-Boron Derivatives Obtained by Various Methods

Method	Bond length in the ring, Å	Angles in the ring		LUMO/HOMO gap energies, eV	Aromaticity	
					NICS	S-NICS
		[10]-Annulene				
CAM-B3LYP/6-31G*	C–C C=C C–H	1.422 1.368 1.08	CCC=129.1 CCC=121.9 CCH=113.3	15.19	–10.91	–10.83
		$B_4N_4H_8^{2-}$				
CAM-B3LYP/cc-pVTZ	B–N B–H N–H	1.445 1.243 1.015	BNB=142.6 NBN=127.4 HBN=116.3 HNB=108.7	18.86	–9.17	–8.25
		[12]-Annulene				
CAM-B3LYP/6-31G*	C–C C=C C–H	1. 448 1. 368 1.09	CCC=129.1 CCC=122.2 HCC=115.7 CCH=113.3	11.29	4.15	4.11
		$B_7N_7H_{14}$-Annulene				
CAM-B3LYP/6-31G* –566.0629872 –161632.1	B–N N–B B–H N–H	1.437 1.445 1.193 1.017	BNB=125.0 NBN=121.7 HNB=116.2 HBN=117.2	26.65	0.09	0.00
		$C_8H_8^{2-}$				
MP4(SDQ)/6-31+G(*d*′)	C–C	1.415, 1.100	135.0, 112.5	22.50	–14.95	–15.85
QCISD(T)/6-31+G(*d*′)	C–C	1.415, 1.08	135.0, 112.5	22.51	–15.11	–15.83
CAM-B3LYP/6-311G	C–C	1.413, 1.099	135.0, 112.5	22.51	–14.87	–15.87
M06-2X/cc-pVDZ	C–C	1.415, 1.05	135.0, 112.5	23.72	–17.59	–15.88
M06-2X/cc-pVTZ	C–C	1.409, 1.094	135.0, 112.5	21.40	–15.90	–15.82

rings of $C_8H_8^0$ are not aromatic and in contrast to C_6H_6 or $C_8H_8^{2-}$, the *p* orbital electrons are localized [47]. Using the virtual or dummy atom (Bq) in the center of rings, the nucleus-independent chemical shift (NICS) has been calculated (Table 1).

NICS is a simple method developed by Schleyer and coworkers, which estimates the absolute magnetic shielding in the center of molecules, the negative NICS value indicates the aromaticity, and the positive value indicates the anti-aromaticity [19]. S-NICS is a statistical method computing NICSs in the viewpoint of probe motions in a sphere of shielding and deshielding spaces of molecular rings [48]. The data on the chemical shift tensor and other NMR components are listed in Table 2. As can be seen, [12]-annulene has positive NICS and S-NICS values that indicate the anti-aromaticity situation, while these values for other variants are negative and the aromaticity and anti-aromaticity sequence is as follows:

a) anti-aromaticity: [12]-annulene > $B_7N_7H_{14}$-annulene;

b) aromaticity: $B_4N_4H_8^{2-}$ < benzene < [10]-annulene < [14]-annulene < $C_8H_8^{2-}$.

Although in some cases, NICS depends on the model of basis sets, but S-NICS (a statistical model) is independent of various basis sets. Therefore, for the mentioned sequences of data, the SNICS confirmation is needed [48].

TABLE 2. Herzfeld–Berger and Haeberlen Convention of NMR Components with CAM-B3LYP/cc-pVDZ of [n]-Annulene (n = 8, 10, 12, and 14) and its Aza-Boron Derivatives Obtained by Various Methods in Comparison with Benzene

Ion and molecule	σ_{11}	σ_{22}	σ_{33}	σ_{iso}	$\sigma_{aniso}\Delta\delta$	κ	Ω	η
[10]-annulene	–4.81	14.54	23.0	10.91	27.93	0.39	27.81	0.53
[12]-annulene	–27.8	–0.93	16.30	–4.15	–35.5	0.22	44.12	0.72
$B_7N_7H_{14}$-annulene	–9.57	4.31	4.96	–0.09	–14.2	0.91	14.53	0.06
[14]-annulene	2.97	3.97	37.92	14.95	34.45	–0.94	34.95	0.05
Benzene C_6H_6	5.55	6.28	13.86	8.56	7.94	–0.82	8.30	0.14
$C_8H_8^{2-}$	3.4	3.4	40.9	15.9	37.6	–0.99	33.7	0.0
$B_4N_4H_8^{2-}$	1.97	1.97	23.57	9.17	21.6	–0.99	21.6	0.0

The ELF current density map from the ab initio calculations of [*n*]-annulene (*n* = 8, 10, 12, and 14) and its aza-boron derivatives are shown in Figs. 1 and 2, and the currents are dominated by HOMO contributions (Table 3). In a ring with the 4*n*+2 system, HOMO–LUMO are related to *n*+1 and *n*, but for a ring with 4*n* electrons, they are derived from a split degenerate ($\lambda = n$). For $n = 4$, λ is zero, meanwhile the diatropic contribution arises from a transition in which $\Delta\lambda = +1$ and the paratropic contribution arises from a transition in which $\Delta\lambda = 0$ [14, 15]. In Huckel′s theory for *N* atoms with equal Coulomb parameters $\{\alpha\}$ and equal resonance parameter, the $\{\pi\}$ energies can easily be calculated by the well-known method [49]. Therefore, for the 4*n*+2 systems (with a higher symmetry) only the HOMO–LUMO transitions are considered (diatropic current), and for the 4*n* ring (lower symmetry) two forms can be considered. The first HOMO–LUMO transition leads to a paratropic contribution, and the second HOMO–LUMO+1 transitions leads to diatropic contributions [49].

Since in the closed shell of the 4*n*+2 systems, the occupied orbitals appear in the complete shells, in the plane rotation only orbitals with the same $\{\lambda\}$ can overlap, and it cannot occur from occupied-to-virtual transitions. On the other hand, the mixed adjacent orbitals must differ by $\{\Delta\lambda = \pm 1\}$. The lonely occupied-virtual-translational (OVT) transitions in the (4*n*+2) system are therefore HOMO to LUMO ones, and thus, in this monoring system, the ring current occurs only from the HOMO orbitals which are fully diamagnetic, but for $n = 0$ HOMO is with degeneracy = 2, and the (4*n*+2) system has four electrons in the diamagnetic situation. In 4*n*, the $\{\pi\}$ systems have half-filling of the angular momentums, therefore in the full D_{nh} symmetry, it goes towards to an open-shell configuration with a distorting degeneracy. Via reducing the symmetry, HOMO and LUMO pairs are split into non-degenerate orbitals relevant to a rotational transition with small energy divisors. As can be seen in Table 3, gap energies, HOMO/LUMO overlap values, and HOMO/HOMO–1 overlap values in whole spaces obey the sequences that can be considered as (1) HOMO/LUMO overlap values as an index for aromaticity (2) and the HOMO/HOMO–1 overlap as an index for anti-aromaticity.

These HOMO/LUMO overlaps indicate the sum over states, producing a strong two-electron paramagnetic ring current. Other rotational and translational transitions are presented through the symmetry lowering and are actually not important in small cycles. $C_8H_8^{2-}$ and $B_4N_4H_8^{2-}$ are structured with σ/σ^* orbitals around π/π^* molecular orbitals where the overlap of the σ/π separation was missed. On the other hand, for the systems such as $B_4N_4H_8^{2-}$ with the heterocycle orbitals the localization under a large electronegativity will normally lead to the loss of the ring current (Fig. 1).

In Table 4, the ring perimeter sequences for two series are dependent, firstly, on the number of π electrons, and secondly, the number of π orbitals. Therefore, for these compounds, it is needed to rearrange the Coulomb and resonance integral equations as (1); boron and nitrogen atoms are zero- and two-electron donors with $(\alpha–\beta)$ and $(\alpha+1.5\beta)$ orbital energies for them, respectively. Therefore, in the structure of these molecules with different electronegativities of boron and nitrogen atoms, a symmetric change to the Coulomb parameters yield $(\alpha–\gamma\beta)$ and $(\alpha+\gamma\beta)$ energies where γ is a correlated parameter in various structures and varies between $0 \le \gamma < 1$. The solution of the Huckel equation via considering the γ parameter with a simple modification gives molecular orbitals $\{\varnothing\}$ and related energies $\{\varepsilon\}$ from which the consequences for

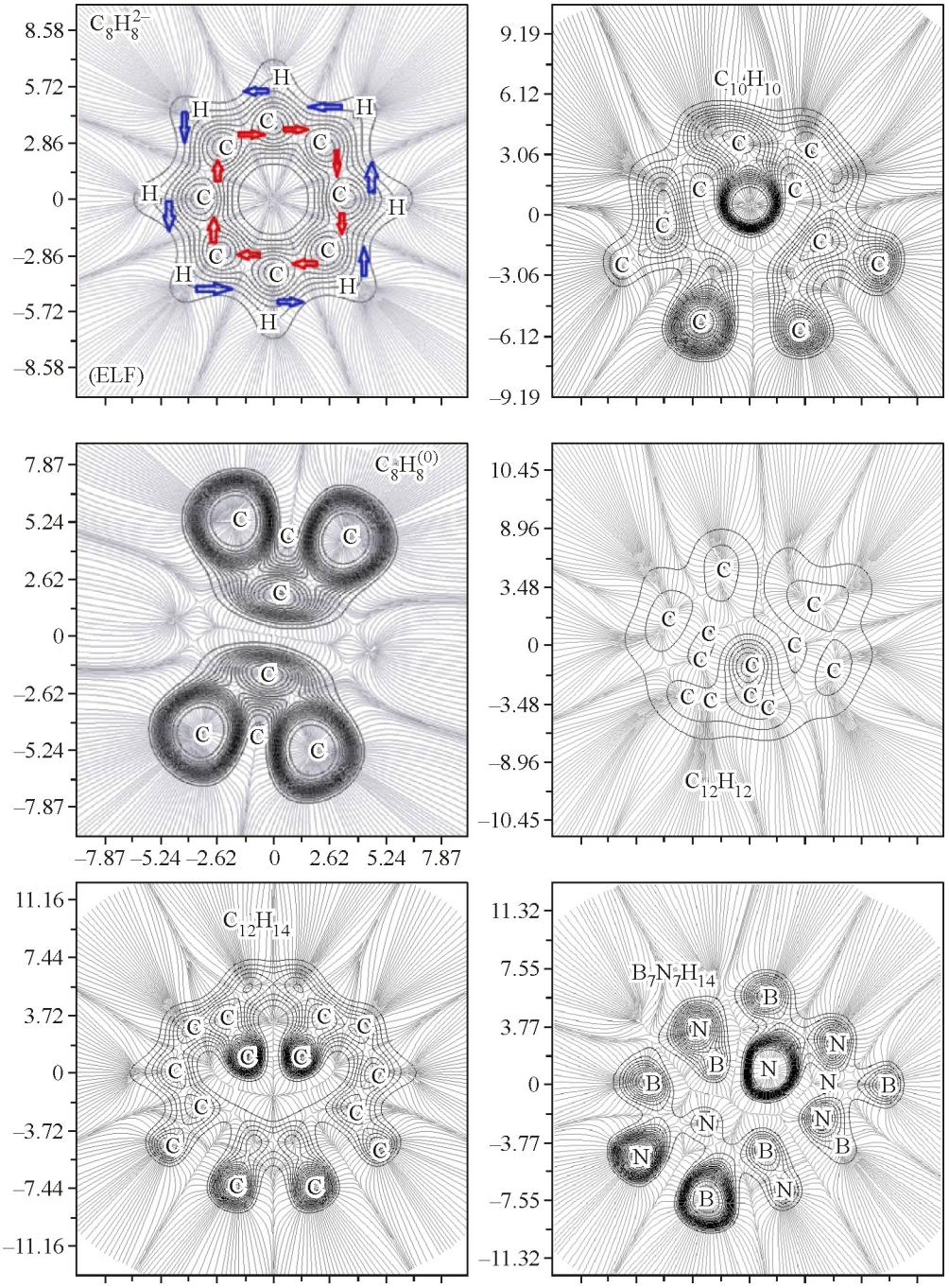

Fig. 1. Gradient line map of ELF and induced current density of [*n*]-annulene (*n* = 8, 10, 12, and 14) and its aza-boron derivatives such as $B_7N_7H_{14}$. Anticlockwise circulations are diatropic, clockwise circulations are paratropic.

cycle currents can be deduced. Canonical molecular orbitals ($\Psi_{\lambda,c}$) are delocalized with $\gamma = 0$ and in each $\gamma \neq 0$ position a linear combination of these sets can be written for the orbitals. In the fully symmetrical carbocyclic systems, the degeneracy of Ψ_{2c} and Ψ_{2s} can be stabilized by several ways, such as a D_{2d} to D_{4h} distortion of the geometries of "clamped"-replaced COT systems [50].

Due to its bond alternation, D_{4h} COT keeps delocalized orbitals and also the cycle current of the equilateral carbocyclic compound (Fig. 1). In the heterocyclic systems ($\gamma \neq 0$), Ψ_{2c} and Ψ_{2s} are bonding and anti-bonding wave functions which belong to the B_{1u} and B_{2u} symmetric orbitals on the D_{4h} subunits of the D_{8h} character. It is notable that Ψ_{2c} and wave

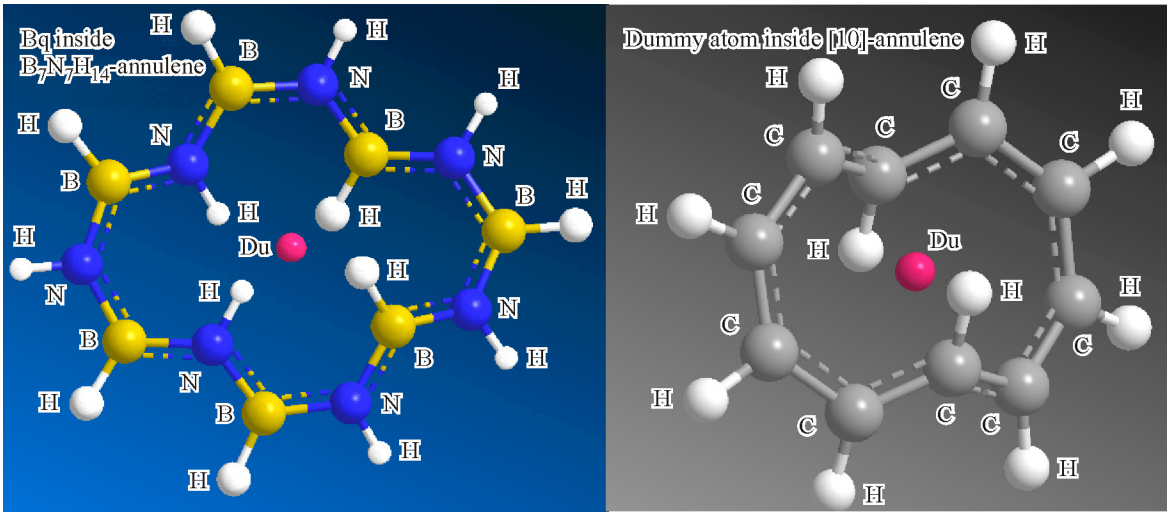

Fig. 2. Optimized structure with a dummy atom (Bq) of [10]-annulene and $B_7N_7H_{14}$-annulene.

TABLE 3. Gap energies, Coefficient of Atomic Orbitals to the Molecular Orbitals for HOMO and LUMO and Their Overlap in the Whole Space for Various Annulenes (by SCPA Partition Method of Stout-Politzer) [51]

Ion & Molecule	Gap energy, eV	Coefficient of atomic orbitals to the molecular orbital of HOMO	Coefficient of atomic orbitals to the molecular orbital of LUMO	HOMO/LUMO overlap in whole space	HOMO/HOMO–1 overlap in whole space
$B_4N_4H_8^{2-}$	3.54	25.0(B1+B4+B6+B7) The coefficient of all hydrogen atoms is zero	6.8(B1+B4+B6+B7)+ +11.5(N2+N3+N5+N8)– –2.6(H9+H12+H14+H15)– –9.4(H10+H11+H13+H16)	0.348	0.338
$B_7N_7H_{14}$-annulene	6.37			0.425	0.590
$C_8H_8^{2-}$	5.38	7.0(C1+C3+C5+C7)+ +17.9(C2+C4+C6+C8) The coefficient of all hydrogen atoms is zero	14.9(C1+C3+C5+C7)+ +16.7(C2+C4+C6+C8)– –3.47(H9+H11+H13+H15)– –3.15(H10+H12+H14+H16)	0.377	0.762
[12]-annulene	2.69			0.807	0.826
[10]-annulene	3.63	11.21(C1+C2)+ +8.23(C3+C10)+ +19.0(C4+C9)+ +7.34(C6+C7)+ +1.7(C5+C8)	16.14(C1+C2)+ +6.3(C3+C10)+ +12.1(C4+C9)+ +9.93(C6+C7)+ +1.6(C5+C8)	0.848	0.668
[14]-annulene	3.23	13.55(C1+C2)+ +0.43(C5+C6)+ +35.13(C9+C10)+ +0.05(C3+C4+C7+C8+ +C11+C12+C13+C14)	5.6(C1+C2)+ +10.8(C3+C4+C8+C11)+ +14.8(C6+C13)+ +0.6(C5+C7+C9+ +C12+C14)	0.892	0.631

TABLE 4. Ring Perimeter, Para-Delocalization (PDI) and Para-Linear Response Indices (PLR) of [n]-Annulene (n = 8, 10, 12, and 14) and its Aza-Boron Derivatives

Molecule	Ring perimeter, Å	PDI	PLR
$C_8H_8^{2-}$	11.30	0.030	0.13
$C_8H_8^0$	11.24	0.032	0.086
$B_4N_4H_8^{2-}$	11.56	0.031	0.16
[10]-annulene	14.07	0.062	0.474
[12]-annulene	16.9	0.0313	0.223
[14]-annulene	23.40	0.074	0.110
$B_7N_7H_{14}$-annulene	23.98	0.064	0.121

functions are HOMO and LUMO for all γ values, which are completely localized. Therefore, HOMO is on the nitrogen atom and LUMO is on the boron atom. Obviously, $\varnothing_{0,c}$, $\varnothing_{1,c}$, $\varnothing_{1,s}$, $\varnothing_{3,c}$, $\varnothing_{3,s}$, and $\varnothing_{4,c}$ become strongly localized on the electronegative atoms. When γ = 1, the nitrogen and boron atoms obey Huckel′s population as $1 \pm \frac{1}{2}\left(\frac{1}{2} + \frac{1}{\sqrt{3}} + \frac{1}{2\sqrt{5}}\right) \approx 1.66$ and 0.36 electrons, respectively. In the Huckel–London approach, the ring current of the eight-membered ring for small γ, the HOMO–LUMO contribution overcomes the bond–bond polarizability. By increasing γ from planar-constrained COT (where γ = 0) to planar $B_4N_4H_8$ (where γ = 1), the eight-membered ring has still a net paratropic circulation. The symmetry reduces the system to the $4n\pi$ position overmatched via the HOMO–LUMO transitions amongst small gap energies. This situation ($\Delta\lambda = 0$) generates intense and paratropic intensities. In other words, the symmetry reasoning for deducing the currents in $4n$ systems consist of several levels (γ = 0). The current is under the HOMO–LUMO transition with a small energy gap towards γ = 1. The HOMO–LUMO gap opens, and the intensities of the current fall but it remains paramagnetic. Here the separation of HOMO–1 and LUMO as well as HOMO and LUMO+1 increase slowly and the paratropic or anti-aromatic cycle current is reduced significantly (Tables 2 and 3). The investigation of the symmetry can be performed for understanding ring and perimeter currents in those systems. Ring perimeters (Å) and the areas ($Å^2$) of those molecules are listed in Table 3. Based on these data, the ring perimeters and the area values are not linearly related due to the non-geometrical behavior of aromaticity in heteromolecules, including boron and nitrogen.

In Table 4, the aromatic fluctuation index for aromaticity is close to zero and the delocalization index is acceptable for those systems, and PLR for aromaticity is larger than that for anti-aromaticity. As can be seen from Table 3, the HOMO coefficient of all hydrogen atoms are zero or close to zero (the coefficient of atomic orbitals to the molecular orbital for HOMO orbitals), and also in some molecules, these coefficients for some atoms in the rings are zero, for instance (C3+C7). In contrast, for LUMO the hydrogen atom plays a considerable role in the percentage of composition, therefore the gap energies are related to the number of hydrogen atoms, which, fortunately, here for all variants are equal, which means that HOMO, LUMO, and gap energies are dependent only on the ring situation in viewpoints of aromaticity, anti-aromaticity, and induced currents.

Based on the NBO analysis (Tables 5-7), the NHO direction and bond bending (deviations from the line of nuclear centers) can be estimated for understanding the situation with π and σ orbitals. These data are often useful for predicting the direction of geometry changes resulting from the geometry optimization. The direction of a hybrid is specified in terms of the polar (θ) and azimuthal (φ) angles of the vector describing its *p* component. The hybrid directions are then compared with the direction of the lines between the centers of two nuclei for determining the bending of those bonds expressed as the deviation angles between these two directions. For $C_8H_8^{2-}$, $B_4N_4H_8^0$, and $C_8H_8^{2+}$, NBO calculations exhibit that these structures are the dominant Lewis structures. However, based on the advanced valence bond theory, covalent-ionic resonances are not necessary due to the inclusion of bond polarity effects in a resonance structure. By this work, for each of NAO functions (core, valence, or Rydberg) the orbital occupancy and the orbital energy are shown, and it is notable that the occupancies of Rydberg (Ryd) NAOs are typically much lower than those of core and valence (Val) NAOs of the natural minimum basis (NMB) set.

TABLE 5. NHO Direction and Bond Bending Deviations from the Line Between Nuclear Centers in Variants of $[B_nN_nC_{(8-2n)}H_8$ (n = 2, 4)]

NBO	Line between centers		Hybride 1			Hybride 2			Wave function	OCC
	θ	φ	θ	φ	Dev	φ	θ	Dev		
						$B_4N_4H_8^{2-}$				
B1–N2 (σ)	90.0	107.6	90.0	104.5	3.1	90.0	290.4	2.8	0.47 $sp^{2.06}$ of B1 + 0.88 $sp^{1.37}$ of N2	1.98
B1–N3 (π)	90.0	340.2	0.0	0.0	90.0	0.0	0.0	90.0	0.45 P^1 of B1 + 0.89 P^1 of N3	1.98
N2–B4 (π)	90.0	70.2	0.0	0.0	90.0	0.0	0.0	90.0	0.45 P^1 of B4 + 0.89 P^1 of N2	1.98
N2–B4 (σ)	90.0	70.2	90.0	67.4	2.8	90.0	253.3	3.1	0.47 $sp^{2.06}$ of B4 + 0.88 $sp^{1.37}$ of N2	1.88
N3–B6 (σ)	90.0	17.6	90.0	20.4	2.8	90.0	194.5	3.1	0.47 $sp^{2.06}$ of B6 + 0.88 $sp^{1.37}$ of N3	1.98
N5–B7 (π)	90.0	340.2	0.0	0.0	90.0	0.0	0.0	90.0	0.45 P^1 of B7 + 0.89 P^1 of N5	1.88
						$B_4N_4H_8^0$				
N1–B2 (σ)	90.1	69.0	90.0	65.7	3.3	89.9	252.5	3.6	0.47 $sp^{2.06}$ of B1 + 0.88 $sp^{1.46}$ of N2	1.98
N1–B2 (π)	90.1	69.0	0.1	352.6	90.1	179.9	230.3	90.0	0.31 P^1 of B4 + 0.94 P^1 of N2	1.88
N1–B2 (π*)	90.1	69.0	0.1	352.6	90.1	179.9	230.3	90.0	0.31 P^1 of N1* + 0.94 P^1 of B2*	0.166
B2–N4 (σ)	90.1	18.2	90.1	14.7	3.6	90.0	201.5	3.3	0.47 $sp^{2.06}$ of B2 + 0.88 $sp^{1.46}$ of N4	1.98
N6–B3 (π)	90.1	333.9	0.1	308.5	90.0	0.1	242.2	89.9	0.31 P^1 of B3 + 0.94 P^1 of N6	1.83

TABLE 6. Occupancy Threshold for a Suitable Pair, Total Populations of Lewis and non-Lewis Structures, Number of Core (CR), 2-Center Bond (BD), Lone Pair (LP) NBOs in the Natural Lewis Structure, Number of Low-Occupancy Lewis (L) and High-Occupancy (> 0.1e) non-Lewis (NL) Orbitals, and Maximum Deviation (Dev) of Any Formal Bond Order for the Structure From a Nominal Estimate (NAO Wiberg Bond Index) for Several Compounds.

Compound	Threshold	Lewis	Non-Lewis	CR	BD	LP	(L)	(NL)	Dev
$B_2N_2C_4H_8^{(0)}$	1.90	55.4	0.6	8	20	0	0	1	0.04
$B_4N_4H_8^{(0)}$	1.90	54.4	1.6	8	16	4	4	4	0.03
$B_4N_4H_8^{(2-))}$	1.90	55.0	2.9	8	16	5	5	3	0.17
$C_8H_8^{(0)}$	1.90	55.3	0.7	8	20	0	0	0	0.05
$C_8H_8^{(2-)}$	1.90	53.8	4.2	8	16	5	5	3	0.36

TABLE 7. Donors and Acceptors of Some Bonds in $B_4N_4H_8^{(0)}$

Donor NBO (i)	Acceptor NBO (j)	E^2, kcal/mol	$E_j - E_i$, a.u.	$F_{i,j}$, a.u.
N1–B2 (σ)	(N1–H9)*	2.03	1.28	0.45
N1–B2 (π)	RY*B3	1.18	1.49	0.039
N1–B2 (π)	(B3–N6)*	50.21	0.43	0.132
N1–B2 (π)	(N1–B2)*	1.38	0.43	0.022

In addition, the occupancy threshold for a sufficient estimation, total populations of Lewis and non-Lewis NBOs, the number of core (CR), 2-center bond (BD), 3-center bond (3C), and lone pair (LP) NBOs in the natural Lewis structure, the number of low-occupancy Lewis (L) and high- occupancy non-Lewis (NL) orbitals, and the maximum deviation (Dev) of any formal bond order for the structure from a nominal estimate have been considered for $C_8H_8^{2-}$, $C_8H_8^{2+}$, $B_2N_2C_4H_8^0$, $B_2N_2C_4H_8^{2-}$, and $B_4N_4H_8^{2-}$ (see Supplementary). For instance, in $B_4N_4H_8^{-2}$ (Table 5), the NHO nitrogen atom of the B1–N2

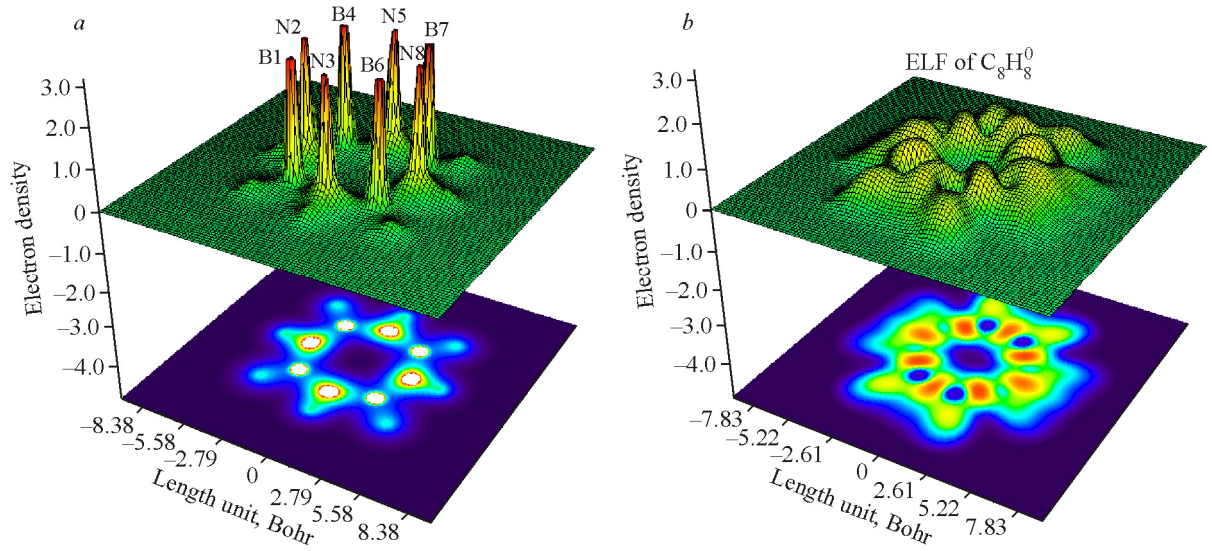

Fig. 3. Shaded surface map with a projection of the density of state of $B_4N_4H_8^{2-}$: ELF total electron density (*a*), LOL density of $C_8H_8^0$ (*b*).

(σ) bond is bent away from the line of B–N centers by 3.1° for Hybrid 1 and 2.8 for Hybrid 2. The N–H bonds of B1–N3 (π) are bent by even 90.0, which indicates pure (π). The information in these tables is a brief of all calculations, therefore, for any further information the output files of NBO, NMR, and optimization of those variants are presented in the of Supplementary Materials.

For instance, in Table 7, the N_1–B_2 (π) → (B3–N6)* interaction between the N_1–B_2 bonding and the planar (B3–N6)* anti-bond is seen to give a strong stabilization of 50.21 kcal/mol with the F matrix of 0.132.

A symmetrical distribution of electron densities and LOL densities, including DOS, PDOS, TDOS and OPDOS for $B_4N_4H_8^{2-}$, can be seen in Fig. 3, which indicates isostructures between these two compounds and $C_8H_8^{2-}$ (Fig. 4).

Through NBO and the Multiwfn software, for each molecule the maps indicate total *p* and *s* contributions for inducing current densities. As expected, the currents from the *p* electrons are strongly diatropic in benzene and strongly paratropic in COT (Figs. 3-5). The currents are overmatched by HOMO contributions in both cases. The angular-momentum analysis exhibits how the symmetry rules account for these aspects. At each consecutive energy level, quantum number *l* (0, 1, …, *N*/2) increases by one. In a cycle with $N = 4n+2$ electrons, HOMO and LUMO correspond to $n = \alpha$ and $n = \alpha + 1$, respectively. It is notable that photo-excited COT relaxes toward the planar D_{8h} symmetry, and its structure appears to be identical to the thermal double bond shift transition state. This is the typical π-delocalized structure expected to characterize a Huckel anti-aromatic [4*n*] system. As can be seen in Tables 3 and 4 (coefficient of atomic orbitals to the molecular orbital of HOMO, LUMO, and HOMO–1) some electrons are localized and some others are not on the aza-boron heterocycle variants. For benzene the low energies may only involve one delocalized allyl radical and three adjacent unpaired electrons while in COT, due to its larger size, a new and more stable tetraradical-type configuration might be possible.

Total densities of states of these molecules and ions are plotted in Fig. 3 and 4. As can be seen, the energies for all systems are distributed between –0.8 a.u. up to 0.2 a.u. For $B_4N_4H_8^0$, $C_8H_8^0$, $B_2N_2C_4H_8^{2-}$ molecules which exhibit anti-aromaticity, the densities in the energy ranges from –0.2 up to 0.0 are zero, while for those molecules with the aromaticity behavior are not.

LOL for the variants of $B_4N_4H_8^{2-}$ and $C_8H_8^{2-}$ bonds are plotted in Fig. 5. The locations of sharp peaks and also the distances between two sharp peaks in each bond are related to (σ) or (π) bonds. COTs have extended delocalized structures (i.e., identical 1.40 Å (π)-bonds and planarity, recalling an aromatic system).

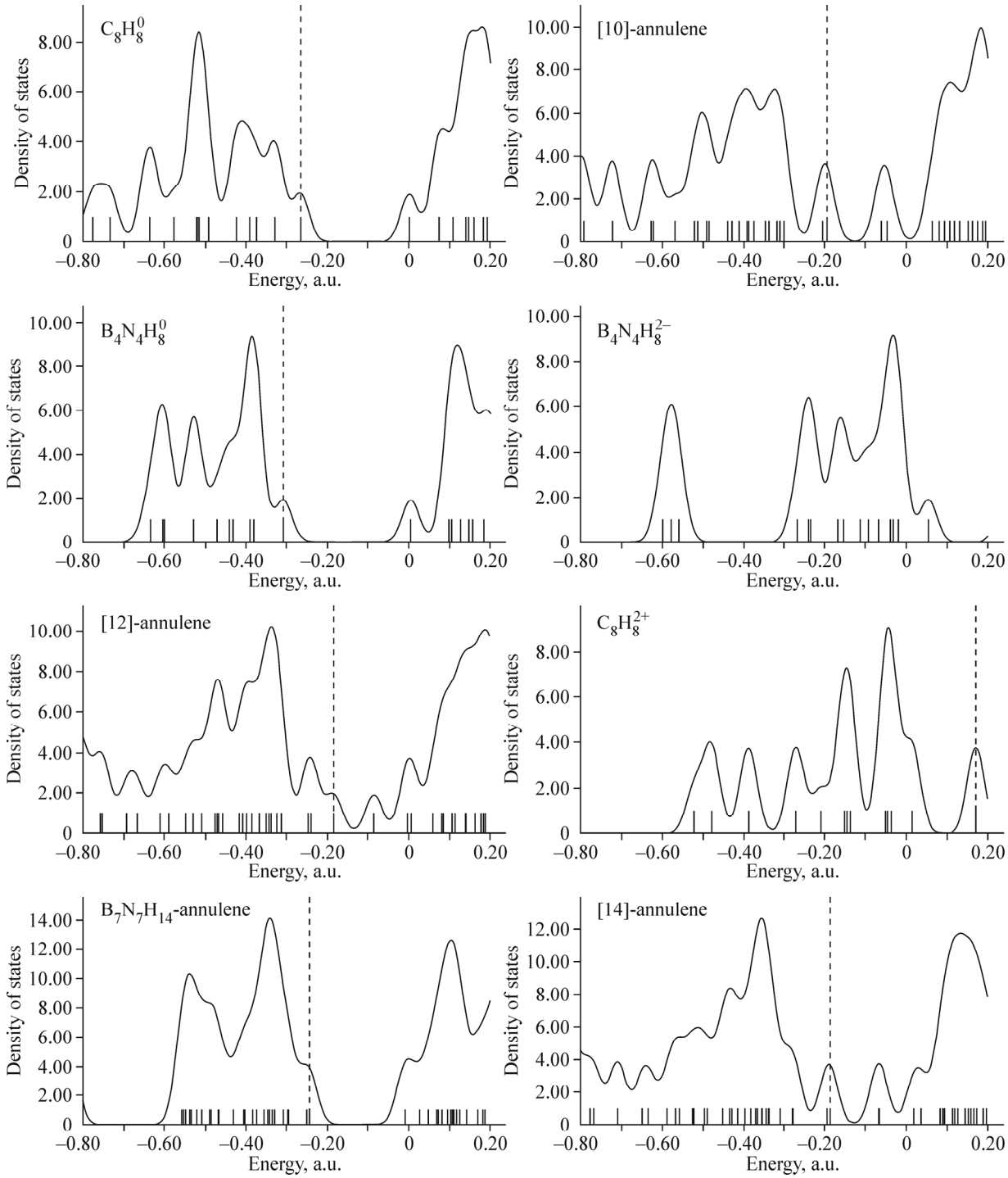

Fig. 4. Total density of states of [*n*]-annulene (*n* = 8, 10, 12, and 14) and its aza-boron derivatives such as $B_4N_4H_8$ and $B_7N_7H_{14}$.

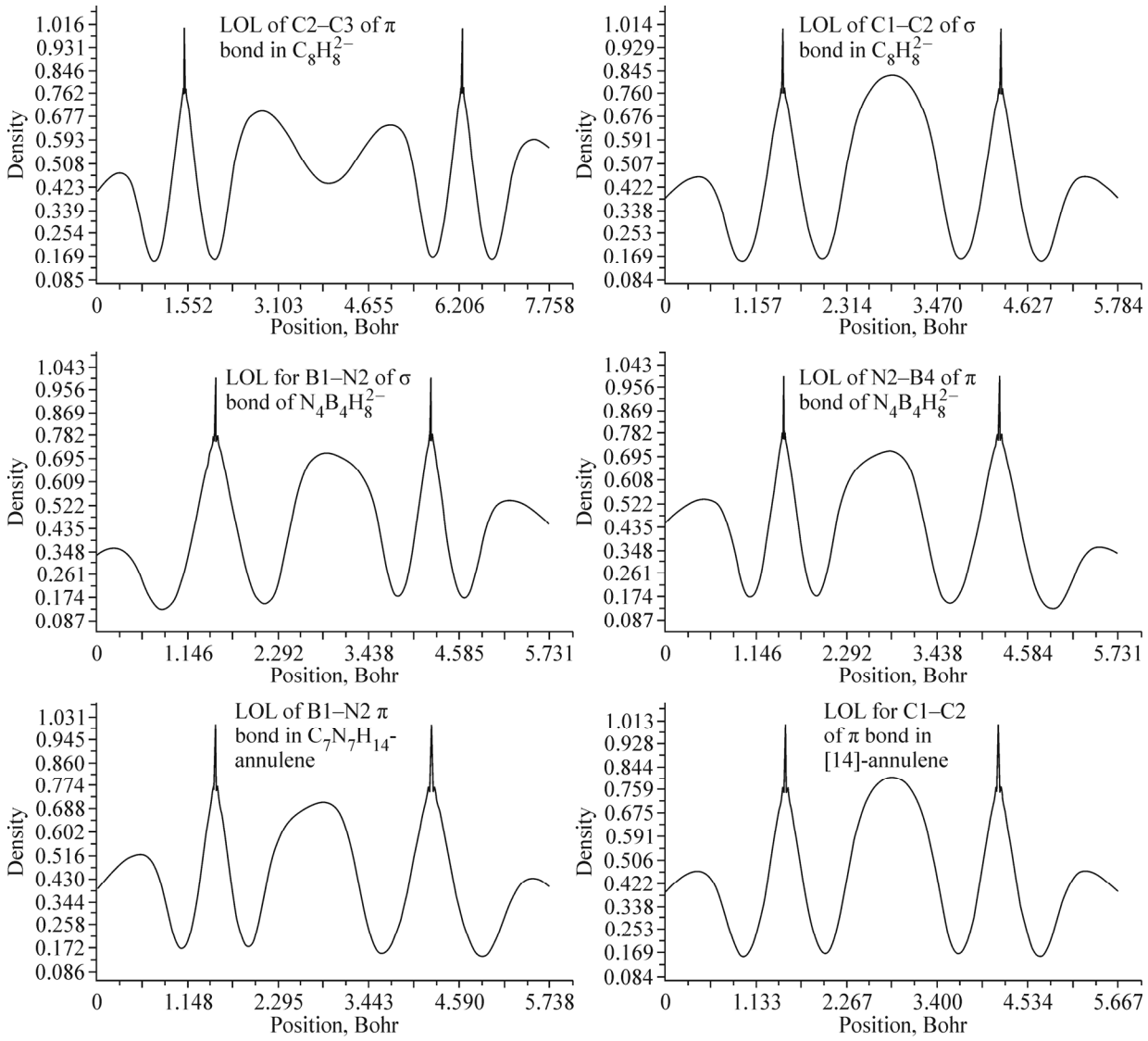

Fig. 5. LOL of [*n*]-annulene (*n* = 8 and 14) and its aza-boron derivatives such as $B_4N_4H_8$ and $B_7N_7H_{14}$.

Therefore, it can be considered that COT is stabilized by a kind of aromatic effects, which plays against the out-of-plane deformation needed to reach both *boat* and kink structures due to those motions, and the delocalization is broken. The calculations of charges and bond orders for several variants of $C_8H_8^{n+2}$ (*n* = –6, –4, –2, 0) are plotted in Fig. 5. Since the bond orders are the integer numbers of chemical bonds, in molecules that have resonance or non-classical bondings, the bond order may not be an integer. In other words, the delocalized molecular orbitals contain π orbitals essentially yielding half a π together with the σ bond bonds for each pair of atoms. However, generally, a calculated

bond order that is not 1.5 depends on complex scenarios and essentially refers to the bond strength relative to single order bonds. Wiberg′s and Fuzzy′s bond order methods correspond to molecules with anti-aromatic and aromatic properties, respectively. Since the magnitude of the bond order is asso ciated with the bond length, the situation of LOL bonds have been calculated and estimated for any further analysis (Fig. 5).

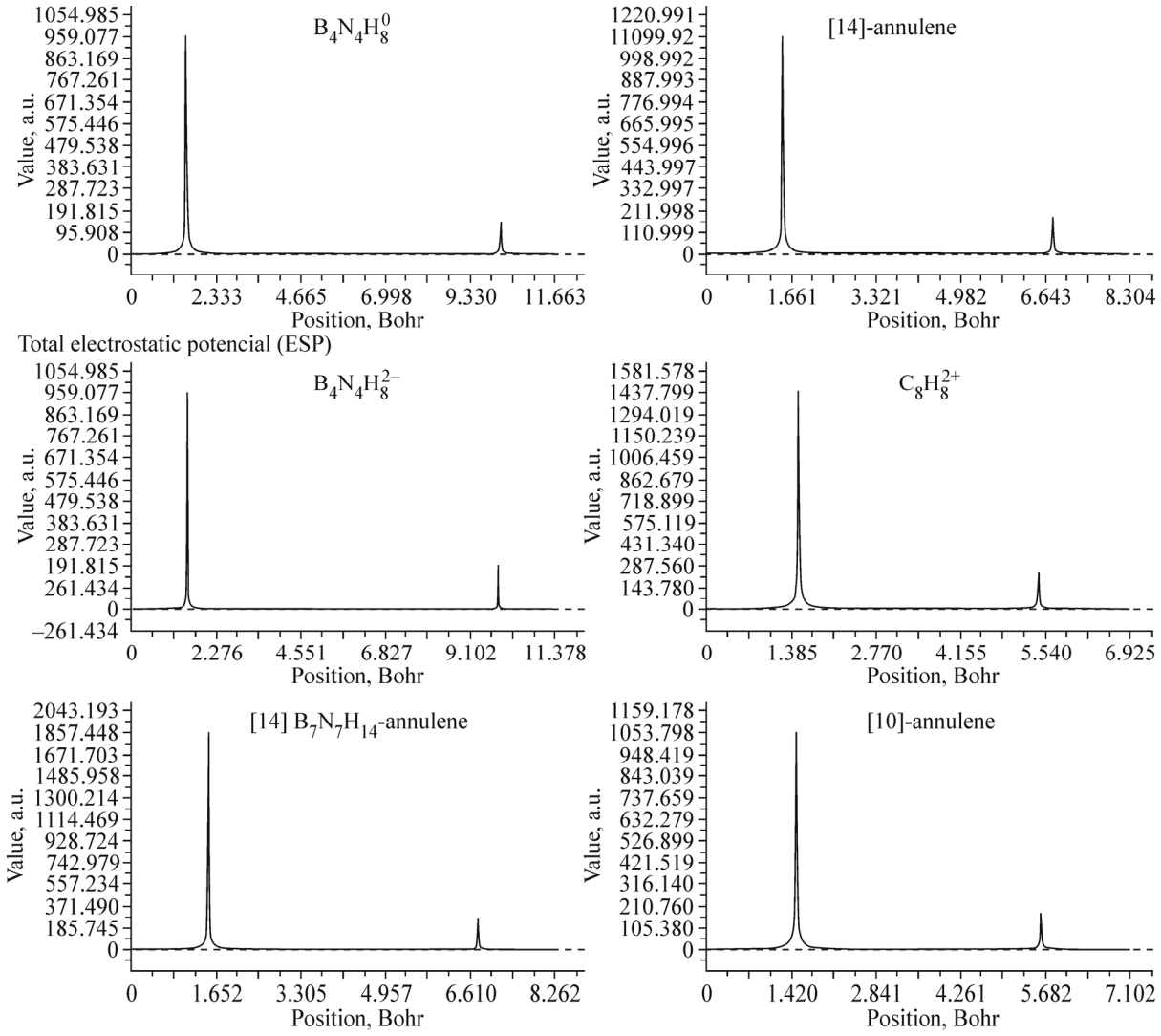

Fig. 6. Total electrostatic potential for variants of [*n*]-annulene (*n* = 8, 10 and 14) and its aza-boron derivatives such as $B_4N_4H_8$ and $B_7N_7H_{14}$.

As can be seen in Fig. 6, the stable electrostatic for those variants are started around the bond length positions. The total electrostatic potential for $B_4N_4H_8^0$, $B_2N_2C_4H_8^{2-}$, $B_4N_4H_8^{4-}$, and $C_8H_8^{2+}$ variants are shown in Fig. 6 where sharp peaks are located at 1.166, 1.127, 1.138, and 1.385, respectively.

CONCLUSIONS

Current-density maps, ELF and LOL from ab initio calculations for $C_8H_8^{n+2}$ ($n = -4, -2, 0$) and $B_nN_nC_{8-2n}H_8$ ($n = 2, 4$) are investigated as a novel method for understanding the aromaticity and the anti-aromaticity in heterocyclic compounds. For each molecule, the maps indicate total *p* and *s* contributions for inducing current density. As expected, the currents arising from *p* electrons are, respectively, strongly diatropic in benzene and strongly paratropic in COT. An angular-momentum analysis shows the symmetry rules for these aspects. The currents are dominated by HOMO contributions in both cases. An angular-momentum analysis shows how the symmetry rules account for these features. The HOMO/LUMO overlap in whole spaces indicates the sum over states, producing a strong two-electron paramagnetic ring current. Other rotational and translational transitions presented through the symmetry lowering actually are not important in small cycles. The anti-aromaticity is a result of the HOMO/HOMO-1 overlap in whole spaces.

ACKNOWLEDGMENTS

Our common idea and preliminary discussion of this work refer to the duration of my sabbatical collaborating with professor James E. Boggs (who passed away) in the Institute for Theoretical Chemistry, Department of Chemistry and Biochemistry, The University of Texas at Austin, Austin, Texas, United States that reminds me his memory.

CONFLICT OF INTERESTS

The authors declare that they have no conflict of interests.

REFERENCES

1. P. Willstätter, E. Waser, and R. Willstätter. *Ber. Dtsch. Chem. Ges*., **1911**, *44*(*3*), 3423–3445.
2. J. F. M. Oth. *Pure Appl*. *Chem*., **1971**, *25*, 573–622.
3. J. I. Wu, I. Fernández, Y. Mo, and P. V. R. Schleyer. *J. Chem*. *Theory Comput*., **2012**, *8*, 1280–1287.
4. R. Naor and Z. Luz. *J. Chem. Phys.*, **1982**, *76*, 5662–5664.
5. J. L. Andrés, O. Castaño, A. Morreale, R. Palmeiro, and R. Gomperts. *J. Chem. Phys.*, **1998**, *108*, 203–207.
6. T. Nishinaga, T. Ohmae, and M. Iyoda. *Symmetry*, **2010**, *2*, 76–97.
7. C. Gellini and P. R. Salvi. *Symmetry*, **2010**, *2*, 1846–1924.
8. P. G. Wenthold, D. A. Hrovat, W. T. Borden, and W. C. Lineberger. *Science*, **1996**, *272*, 1456–1459.
9. A. Schild and B. Paulus. *J. Comput. Chem*., **2013**, *34*, 1393–1397.
10. D. A. Hrovat and W. T. Borden. *J. Am. Chem. Soc*., **1992**, *114*, 5879–5881.
11. C. D. Stevenson, E. C. Brown, D. A. Hrovat, and W. T. Borden. *J. Am. Chem. Soc*., **1998**, *120*, 8864–8867.
12. A. Schild and B. J. Paulus. *J. Comput*. *Chem*., **2013**, *34*, 1393–1397.
13. T. Yoshida and C. Tokizaki. *Chem. Phys. Lett*., **2015**, *634*, 134–139.
14. E. Steiner and P. W. Fowler. *J. Phys*. *Chem*. *A*, **2001**, *105*, 9553–9562.
15. E. Steiner, P. W. Fowler, and R. W.A. Havenith. *J. Phys*. *Chem*. *A*, **2002**, *106*, 7048–7056.
16. F. London. *J. Phys*. *Radium*., **1937**, *8*, 397–409.
17. L. Pauling. *J. Chem*. *Phys*., **1936**, *4*, 673–677.
18. J. A. Pople. *J. Chem*. *Phys*., **1956**, *24*, 1111.
19. P. von R. Schleyer, C. Maerker, A. Dransfeld, H. Jiao, and N. J. R. van Eikema Hommes. *J. Am*. *Chem*. *Soc*., **1996**, *118*, 6317–6318.
20. A. Soncini, P. W. Fowler, and L. W. Jenneskens. *Phys*. *Chem*. *Chem*. *Phys*., **2004**, *6*, 277–284.
21. F. A. L. Anet and D. J. O′Leary. *Concepts Magn*. *Reson*., **1992**, *4*, 35.
22. U. Haeberlen. In: Advances in Magnetic Resonance. Suppl. 1. Academic Press: New York, **1976**.
23. M. Mehring. High Resolution NMR Spectroscopy in Solids, 2nd. Ed. Springer Verlag: Berlin, **1983**.
24. NMR Basic Principles and Progress. / Eds. P. Diehl, E. Fluck, and R. Kosfeld. Springer Verlag: Berlin, **1978**, *15*.
25. R. K. Harris, E. D. Becker, S. M. Cabral de Menezes, P. Granger, R. E. Hoffman, and K. W. Zilm. *Ann*. *Magn*. *Reson*., **2008**, *7*, 1.
26. J. Herzfeld and A. E. Berger. *J. Chem*. *Phys*., **1980**, *73*, 6021.
27. R. F. W. Bader. Atoms in Molecule: A quantum Theory. Oxford Univ. Press: Oxford, **1990**.
28. A. D. Becke and K. E. Edgecombe. *J. Chem*. *Phys.*, **1990**, *92*, 5397.
29. A. Savin, O. Jepsen, J. Flad, O. K. Andersen, H. Preuss, and H. G. von Schnering. *Angew*. *Chem*., *Int*. *Ed. Engl*., **1994**, *31*(2), 187.
30. A. D. Becke. *J. Mol*. *Struct*.: *THEOCHEM*, **2000**, *527*, 51.

31. H. Jacobsen. *Can*. *J. Chem*., **2008**, *86*(7), 695–702.
32. W. Kohn and L. J. Sham. *J. Phys*. *Rev*., **1965**, *140*, A1133–1138.
33. J. P. Perdew, K. Burke, and Ernzerhof. *Phys*. *Rev*. *Lett*., **1996**, *77*, 3865–3868.
34. T. Lu and F. Chen. *J. Mol*. *Graph*. *Model*., **2012**, *38*, 314–323.
35. T. Lu and F. Chen. *J. Comp*. *Chem*., **2012**, *33*, 580–592.
36. B. H. Besler, K. M. Merz, and P. A. Kollman. *J. Comp*. *Chem*., **1990**, *11*, 431–439.
37. L. E. Chirlian and M. M. Francl. *J. Comp. Chem*., **1987**, *8*, 894–905.
38. F. Martin and H. Zipse. *J. Comp. Chem*., **2005**, *26*, 97–105.
39. M. Monajjemi, V. S. Lee, M. Khaleghian, B. Honarparvar, and F. Mollaamin. *J. Phys. Chem. C*, **2010**, *114*, 15315.
40. M. Monajjemi and M. Khaleghian. *J. Clust. Sci*., **2011**, *22*, 673–692.
41. M. Monajjemi. *J. Struct*. *Chem*., **2012**, *23*, 551.
42. M. Monajjemi and J. E. Boggs. *J. Phys*. *Chem*. *A*. **2013**, *117*, 1670–1684.
43. M. Monajjemi, W. J. Robert, and J. E. Boggs. *Chem. Phys.*, **2014**, *433*, 1–11.
44. M. Monajjemi, M. Khosravi, B. Honarparvar, and F. Mollaamin. *Int. J. Quantum Chem.*, **2011**, *111*, 2771–2777.
45. M. Monajjemi. *Theor. Chem. Acc.*, **2015**, *134*(77), 1–22.
46. M. Monajjemi. *J. Mol. Model.*, **2014**, *20*, 2507.
47. A. J. Bridgeman. *Polyhedron*, **1998**, *17*, 2279–2288.
48. M. Monajjemi and N. T. Mohammadian. *J. Comput. Theor. Nanosci.*, **2015**, *12*, 4895–4914.
49. A. A. Frost and B. A. Musulin. *J. Chem*. *Phys*., **1953**, *21*, 572.
50. A. Matsuura and K. Komatsu. *J. Am*. *Chem*. *Soc*., **2001**, *123*, 1768–1769.
51. E. W. Stout and P. Politzer. *Theor*. *Chim*. *Acta*, **1968**, *12*(*5*), 379–386.